High-energy-resolution angle-resolved inverse-photoelectron spectroscopy apparatus for damage-free measurements of conduction band structures of functional materials

Yuki Kashimoto[a], Satoshi Ideta[a], Haruki Sato[a], Hibiki Orio[a], Keita Kawamura[a], Hiroyuki Yoshida[a,b,c*]

[a]Graduate School of Science and Engineering, Chiba University, 1-33 Yayoi-cho, Inage-ku, Chiba 263-8522, Japan
[b]Graduate School of Engineering, Chiba University, 1-33 Yayoi-cho, Inage-ku, Chiba 263-8522, Japan
[c]Molecular Chirality Research Center, Chiba University, 1-33 Yayoi-cho, Inage-ku, Chiba 263-8522, Japan

Abstract

The energy band structure of the conduction band (energy-momentum relation of electrons) is crucial to understanding the electron transport of crystalline materials. In this paper, we describe an angle-resolved low-energy inverse photoelectron spectroscopy (AR-LEIPS) apparatus that examines the conduction band structures of materials sensitive to the electron beam, such as organic semiconductors and organic-inorganic hybrid perovskites. The principle of this apparatus is based on angle-resolved inverse photoelectron spectroscopy. To minimize radiation damage and improve energy resolution, we employed our previous approach used in low-energy inverse photoelectron spectroscopy [Yoshida, Chem. Phys. Lett. **539**–**540,** 180 (2012)]. We obtained the overall energy resolution of 0.23 eV with the momentum resolution of 0.9 nm^{-1} at the electron kinetic energy of 2 eV or higher.

*Corresponding author: hyoshida@chiba-u.jp

1. Introduction

The energy-momentum relation (energy band structure) is crucial to understanding the electronic and optical properties of crystalline materials. The valence bands (occupied energy levels, HOMO levels) are routinely investigated by angle-resolved photoelectron spectroscopy (AR-PES).[1] On the other hand, the conduction bands (unoccupied energy levels, LUMO levels) are examined by angle-resolved inverse photoelectron spectroscopy (AR-IPES).[2–4] AR-IPES can be regarded as the inversion process of AR-PES. In inverse photoelectron spectroscopy, a free electron having the kinetic energy E_k is introduced to a sample surface, and a photon $h\nu$ emitted owing to the radiative transition to unoccupied states is detected. From the energy conservation rule, the binding energy E_b is measured with respect to the vacuum level E_{vac} as

$$E_b = h\nu - E_k \quad (\text{from } E_{vac}) \tag{1a}$$

In photoelectron spectroscopy, the binding energy E_b' is also measured with respect to the Fermi level E_F as[1]

$$E_b' = h\nu - E_k - \phi \quad (\text{from } E_F) \tag{1b}$$

where Φ is the workfunction of the sample.

The inverse photoelectron spectrum is obtained by measuring the photon intensity as a function of E_b by scanning either E_k or $h\nu$. To observe the dispersion relation between the momentum k and the energy E_b, the IPES spectra are measured by varying the electron incident angle θ. From the conservation of electron momentum parallel to the sample surface,

$$k_{||} = \frac{\sqrt{2m_0 E_k}}{\hbar}\sin\theta \tag{2}$$

the momentum parallel to the surface $k_{//}$ is obtained, where m_0 and $\hbar$ refer to the electron mass and the reduced Planck constant, respectively. Whereas AR-PES examines the valence band energy as a function of the emitted-photoelectron angle, AR-IPES observes the conduction band energy as a function of the electron incident angle. Although the AR-IPES is often regarded as the time-inversion process of AR-PES, it is not precisely correct because an excess electron (anion) is left in the final state of AR-IPES whereas, an excess hole (cation) is left in AR-PES.

AR-IPES has been applied to metals and inorganic semiconductors to measure the conduction band structures. However, examining the conduction band structures of

molecular systems such as organic semiconductors, adsorbed molecules on a metal surface, and organic-inorganic hybrid perovskite is difficult. This is because the sample tends to be damaged by electron beam bombardment, and the bandwidth is small compared with the energy resolution of AR-IPES. Actually, AR-IPES studies of adsorbed molecules on metal surfaces have been reported,[5–7] although the samples may have been damaged by the irradiation.

The cross-section of IPES is five orders of magnitude smaller than that of PES in the ultraviolet region.[8] The low signal intensity is a fundamental problem of IPES, that is, an intense electron beam of more than 1 μA should be irradiated to the sample surface for a few tens of minutes to several hours to gain a good signal intensity. The weak photon signal is detected using a highly sensitive photon detector specially designed for IPES. Such an intense electron beam bombardment severely damages the molecular samples.[9,10] AR-IPES needs to acquire more than ten different IPES spectra measured at different incident angles θ, which requires an even longer time, from 4 to 20 hours.

Regarding photon detection, a bandpass detector (a gas-filled Geiger-Müller tube[11–21] or an alkali-halide sensitized electron multiplier[22–26] with a halide of an alkali-earth metal plate) or a spectrometer that uses a vacuum-ultraviolet concave grating,[27–35] chromatic aberration of lens[36] or prisms[37] has been employed. The resolutions of these photon detectors seem to be practically limited to 0.32 eV to gain a reasonable signal intensity[18–21] with a few exceptions.[19] As a result, the overall energy resolution of the previous AR-IPES is typically limited to 0.4 eV. The energy resolution required for the conduction band measurements is dependent on the material to be examined. Organic crystals often contain two inequivalent molecules in a unit cell (i.e., herringbone structure) , thereby resulting in the formation of two energetically close sub-bands.[38] In order to resolve the sub-bands, a high energy resolution is desirable. In general, an energy resolution comparable to the bandwidth of the sample is needed.

In 2012, Yoshida developed low-energy inverse photoelectron spectroscopy (LEIPS).[39–41] By lowering the range of E_k below the damage threshold of organic materials of ca. 5 eV,[42,43] damage to organic samples was mostly suppressed. When E_k is reduced, the emitted photon energy also decreases. The electron affinities of organic semiconductors are mostly between 2 and 5 eV.[41,44] The emitted photon is in the UV or visible range (Equation 1). In this energy range, a multilayer bandpass filter combined with a high-sensitivity photomultiplier[39] or a high-resolution spectrometer[45] can be used for photon detection, thereby easily achieving the energy resolution better than 0.1 eV. The overall energy resolution is mainly limited by the energy spread of electron and is

typically 0.25 eV. By resolving the two issues of the previous IPES, the conduction bands of organic semiconductors can be observed with a precision similar to the valence band observation by PES.

Although LEIPS has been successfully applied to various organic materials to determine electron affinities, the angle-resolved measurement using LEIPS is not straightforward. The low-energy electron (E_k below 5 eV) is easily broadened spatially and energetically owing to the space-charge effect. Furthermore, it is susceptible to stray electric and magnetic fields. In the previous LEIPS, electrons with the primary E_k of 10 or 20 eV are generated and decelerated by the bias voltage applied to the sample, as shown in Figure 1a.[39–41] However, when the electron incident angle θ is tilted from the surface normal, the electron beam is deflected because the electric field is disturbed by the sample bias (Figure 1b). For the angle-resolved measurements, we cannot apply the sample bias to the sample. We need to develop an electron gun for electrons with E_k down to ca. 0 eV (Figure 1c). This problem is specific to angle-resolved low-energy inverse photoelectron spectroscopy (AR-LEIPS) because the previous AR-IPES uses electrons with E_k higher than 5 eV, and no sample bias is required.[2]

In this article, we describe the AR-LEIPS apparatus. First, we show an overview of the apparatus. Then, the design strategy and construction of the low-energy electron gun are described. By measuring the image potential state of highly oriented pyrolytic graphite (HOPG), we evaluate the performance of the AR-LEIPS apparatus We particularly focus on the performance in the low-energy region, i.e., between 2 and 5 eV. Finally, we discuss the feasibility of AR-LEIPS measurements of organic samples from the viewpoint of the minimum electron dose to acquire spectra of sufficient quality and the maximum electron dose that does not cause damage to the sample. The practical applications of this apparatus to organic-inorganic hybrid perovskites[46] and organic semiconductors[47] are reported elsewhere.

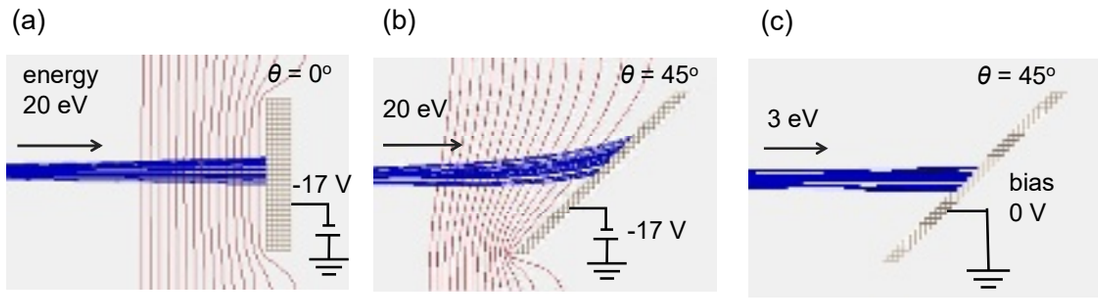

Figure 1. Simulated electron trajectories (blue lines) and equipotential surfaces (red)

for the electron kinetic energy E_k of 3 eV at the sample. (a) Typical conditions for LEIPS without angular resolution (the primary electron kinetic energy of 20 eV, the bias voltage of -17 V, and the sample angle $\theta = 0^o$). (b) Under the same conditions as in (a) except the sample angle that is $\theta = 45^o$. (c) The bias voltage is 0 V and $\theta = 45^o$ for AR-LEIPS. The trajectories were simulated on SIMION8.1 software.

2. Overview of the apparatus

Figure 2 shows the schematic of the AR-LEIPS apparatus. An electron beam from the electron gun is incident on the sample surface. The electron incident angle θ can be changed by rotating the sample angle. The emitted photons are collected and focused onto the photon detector by an ellipsoidal mirror[48] (custom-made SiO_2-coated aluminum mirror, Kiyohara Optics Inc.). The focal lengths of the mirror are f_1 (50 mm) and f_2 (800 mm). The sample is located at f_1, whereas the photon detector is placed at f_2. The mirror diameter of 138 mm results in a solid angle of 4.22 sr for the photon collection. The photon detector consists of a bandpass filter (Semrock, Inc.) and a photomultiplier tube (Hamamatsu Photonics, K.K., R821). The nominal center wavelengths (and determined center energies) of the bandpass filters used in this work are 257 nm (4.83 eV), 300 nm (4.13 eV), 387 nm (3.20 eV), and 434 nm (2.86 eV). The vacuum chamber was evacuated to 3 x 10^{-8} Pa by a turbomolecular pump (pumping speed of 500 Ls^{-1}) and a getter (NEG) pump.

The low-energy electron beam is sensitively affected by the electric and magnetic fields. The external magnetic field (mainly coming from Earth's magnetic field of approximately 50 μT) was shielded by making a vacuum chamber of permalloy, which was further surrounded by a single layer of permalloy metal sheets with a thickness of 1 mm. The magnetic field at the center of the vacuum chamber was smaller than 0.34 μT. As an example, we estimated the effect of the magnetic field on an electron with $E_k = 2$ eV. In Earth's magnetic field of 50 μT, the cyclotron radius was calculated to be 0.1 m. At a distance of 10 mm from the electron source, the electron beam was deflected by an angle of 5.7 deg. In the magnetic field of 0.34 μT, which was realized by magnetic field shielding, the cyclotron radius was increased to 14 m with a reduction of the angle to 0.04 deg. The deflection due to the magnetic field became sufficiently smaller than the initial angular spread of the electron beam $\Delta\theta$ (see Table 1), and the effect of the magnetic field became negligible. The sample holders, the electron gun, and the mirror holders were made of non-magnetic materials such as oxygen-free copper or molybdenum. To shield stray electric fields, the sample was surrounded by a cell made

of oxygen-free copper and beryllium copper meshes. The glass surfaces of the viewports were also covered with metal meshes. To homogenize the electric field, the surfaces of the electrodes of the electron gun, the meshes, and the manipulator were coated with colloidal carbon. The insulators and the electric cables were designed to be hidden from the electron beam. Furthermore, we designed the apparatus to be axially symmetric around the electron beam in order not to disturb the electron beam. For this purpose, the concave mirror was adopted for the photon collection instead of the optical lens used in the previous apparatus. [49]

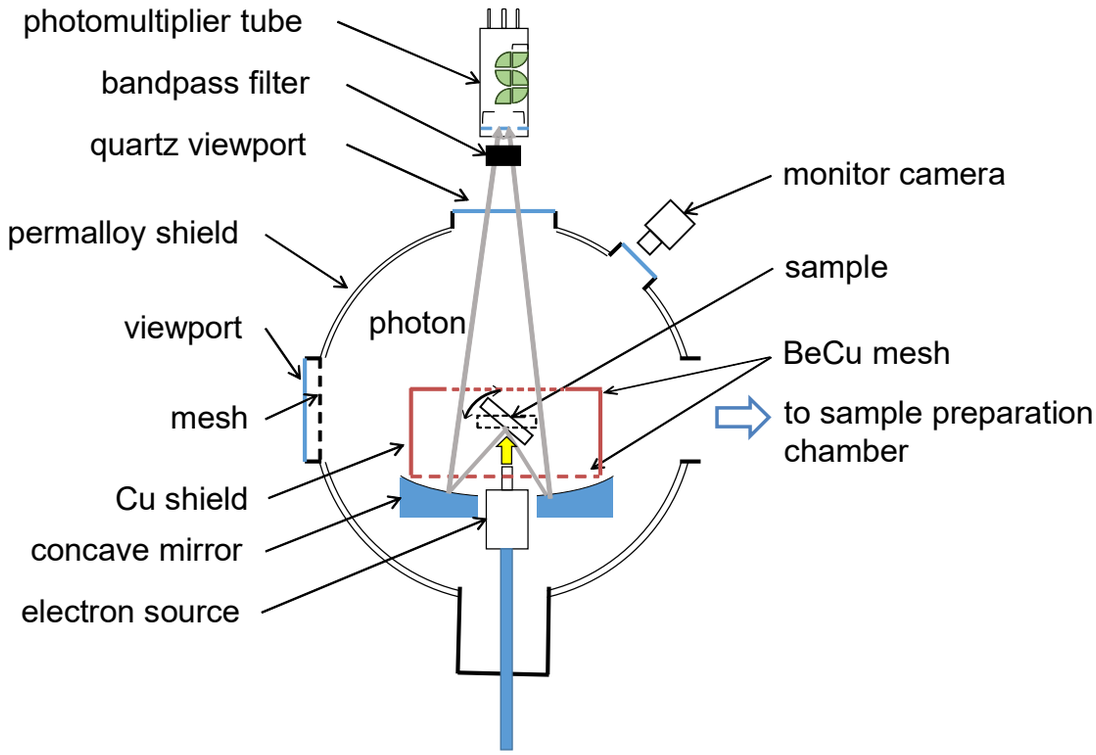

Figure 2. Schematic of the angle-resolved LEIPS apparatus

3. Electron gun

We developed an electron gun that can generate an electron beam with E_k as low as 2 eV while maintaining a sufficient electron current of more than 0.2 μA for AR-LEIPS. The electron gun consists of a hot cathode, an electrode for electron extraction, and an electrostatic lens to focus and decelerate the electron beam.

In previous IPES and LEIPS, the Erdman-Zipf[50] and Stoffel-Johnson[51] types of electron guns equipped with BaO cathodes are widely used because of their high perveance. The

electron is extracted from the BaO cathode by the potential between the cathode V_c and the anode V_a. As the electron current extracted from the cathode is proportional to $(V_a\text{-}V_c)^{3/2}$ owing to the space-charge limit,[52] a sufficiently high potential difference of $e(V_a\text{-}V_c)$ is necessary. We tested a BaO cathode and an aperture with a diameter of 0.5 mm and found that at least 5 eV of $e(V_a\text{-}V_c)$ is necessary to extract the current required for LEIPS.

In the Erdman-Zipf electron gun, $e(V_a\text{-}V_c)$ of $0.4E_k$ is recommended for a planar cathode,[50] whereas in the Stoffel-Johnson electron gun, $6E_k$ is recommended.[51] The Stoffel-Johnson electron gun has the advantage of efficiently extracting electrons at low E_k.[4] For example, $(V_a\text{-}V_c)$ is between 0.1 eV (at E_k = 1 eV) and 0.5 eV (at E_k = 5 eV) in the Erdman-Zipf electron gun, which is not sufficient, whereas $(V_a\text{-}V_c)$ is 6 eV (at E_k = 1 eV) and 30 eV (at E_k = 5 eV) in the Stoffel-Johnson electron gun. However, the emission current is strongly dependent on E_k in the desired energy range of 0 to 5 eV. For the present LEIPS apparatus, we decided to keep $(V_a\text{-}V_c)$ constant, e.g., 5 V.

Then, we designed the electrostatic lens for focusing the electron beam. In place of the three-element electrostatic lens employed in the Erdman-Zipf (an Einzel lens or a uni-potential lens) and the Stoffel-Johnson (a three-element deceleration lens) electron guns, we chose a four-element deceleration lens to increase freedom. The voltages applied to the electrodes were determined on the basis of electron ray-tracing simulation on SIMION 8.1 program. The results are shown in Figure 3.

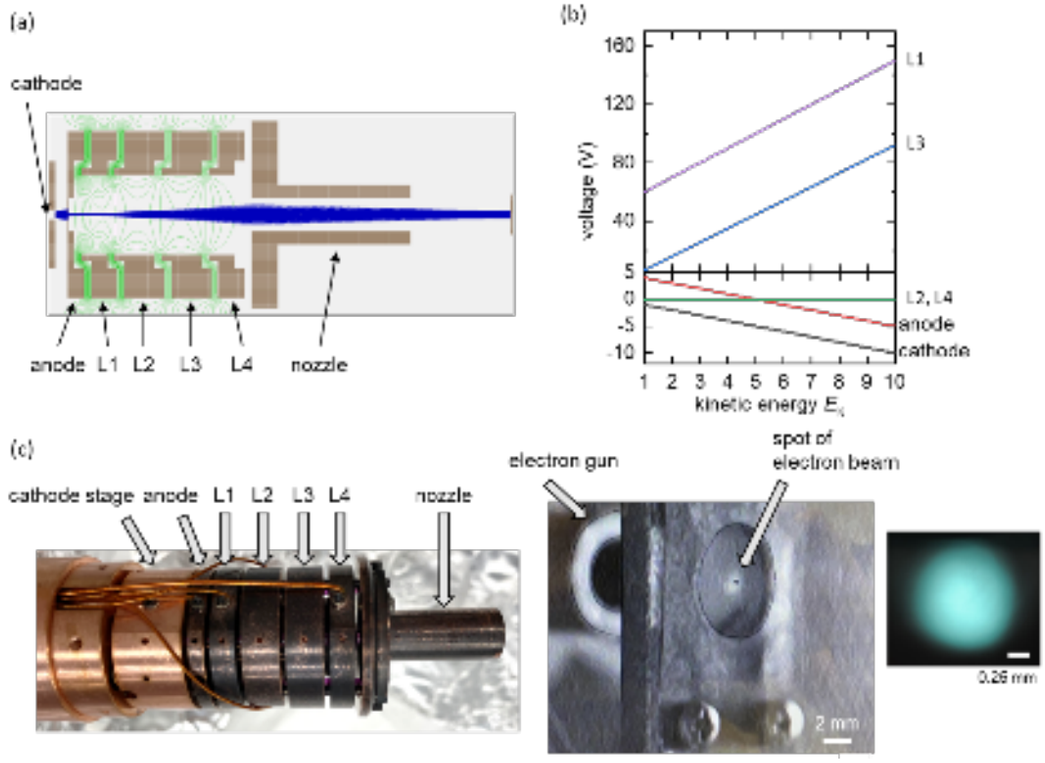

Figure 3. An electron gun developed in this work. (a) Result of electron ray-tracing by SIMION 8.1 showing electrodes, equipotential curves (green lines), and electron trajectories (blue lines). (b) Obtained electrode voltages as a function of desired electron kinetic energy E_k with (V_c-V_a) fixed to 5 eV. (c) Photographs of the electron gun and the spatial distribution of the electron beam appearing on a fluorescence plate.

On the basis of the simulation, we constructed an electron gun. We used the BaO cathode (ES-015, Kimball Physics, Inc.) and positioned the first electrode with a 0.5-mm aperture 1.8 mm downstream. The four lens elements (electrodes, L1–L4 in Figure 3a) with a diameter of 12 mm and a length of 4 mm or 6 mm were made of oxygen-free copper and spaced by 1 mm using ruby balls. After being baked out in a vacuum, we tested the electron gun by measuring the electron current I_{target} at the HOPG target placed 10 mm downstream from the exit of the electron gun using an ammeter (Keithley, 6487 Picoammeter/Voltage Source). The HOPG target was cleaved in air and annealed at 600ºC for 30 minutes in vacuum before the measurement. The power supplies (Kikusui Electronics Corp., PMX-A series and PMC series) were controlled by a PC equipped with a voltage output module (NI-9263) and software coded by the LabView program. The applied voltages were determined from the relation shown in

Figure 3b while taking the workfunctions of the materials into account.

Figure 3c shows the photographs of the electron gun and the spatial distribution of the electron beam that appeared on a fluorescence plate. At the acceleration energy V_c of 9 eV, the diameter of the electron beam was 1.2 mm. At energies lower than 9 eV, the beam diameter was slightly increased even though the fluorescence plate did not emit light. However, the energy and angular distributions were only slightly broadened at a low energy of around 2 eV as discussed later, suggesting that the beam diameter is also increased slightly.

To characterize the energy distribution of the electron beam, we measured the electron current I_{target} as a function of V_c (Figure 4a). By changing the bias voltage V_{bias} applied to the sample, we could characterize the electron beam of different mean energies E_k. The magnitude of V_{bias} was increased from 0 to -14 eV at an increment of -1.0 eV. The maximum I_{target} as a function of V_{bias} is shown in Figure 4c. I_{target} could be tuned by changing the extraction voltage (V_a-V_c). When the electron extraction voltage (V_a-V_c) was 9.5, 6.6, or 4.8 V, a maximum I_{target} of 0.9 μA, 0.2 μA, or 0.03 μA was obtained, respectively, as shown in Figure 4c.

Figure 4b shows the first derivative of I_{target} with respect to V_c from which we evaluated the mean energy and the energy spread of the electron beam. The full width at half-maximum (FWHM) of the energy spread of electron ΔE_k was approximately 0.2 eV and slightly increased with an increase of E_k, as shown in Figure 4d (a precise analysis of ΔE_k will be given later). We expected a higher energy spread at a higher I_{target} owing to the space-charge effect. However, ΔE_k showed no dependence on the extraction voltage (V_a - V_c) in the range between 9.5 V (I_{target} 0.9 μA) and 4.8 V (I_{target} 0.03 μA).

The peak energies of the first derivative of I_{target} are shown in Figure 4e as a function of V_{bias}. The peak energy changed linearly with V_{bias} with the slope of unity until 2 eV. Below 1 eV, the peak energy gradually deviated from the linear relation, suggesting that the electron beam is well-collimated above 2 eV. The peak energy was approximately 2 eV lower than the acceleration potential -V_c owing to the workfunction difference between the BaO cathode (approx. 2.5 eV) and the HOPG (approx. 4.5 eV). It was found that the peak energy deviated from the linear relation below 3 eV when I_{target} exceeded 0.9 μA, likely indicating the space-charge effect. Conversely, the similarity of the curves between 0.03 μA and 0.2 μA indicated that the space-charge effect was negligible in this I_{target} range. We conclude that a well-characterized electron beam is obtained with the energy E_k ranging from 2 eV to 10 eV and the current I_{target} below 0.2 μA. The lowest energy (deepest energy) accessible by AR-LEIPS is limited to 2 eV smaller than the photon energy ($h\nu - 2$ eV) with respect to the vacuum level.

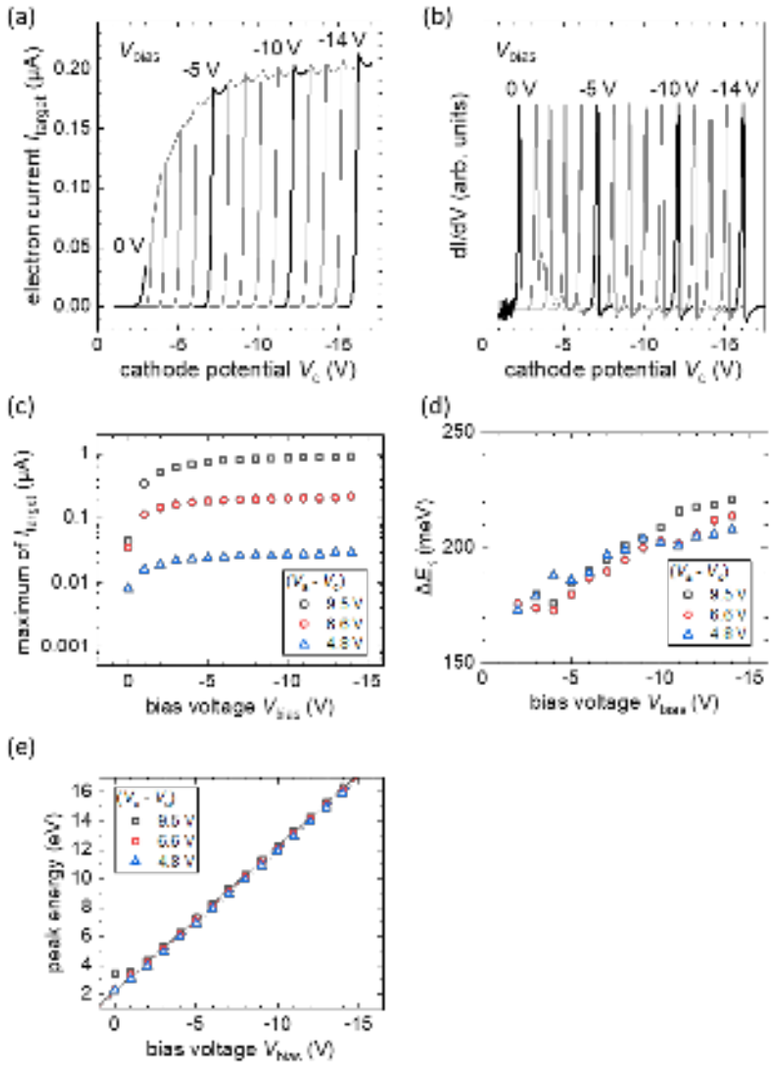

Figure 4. Measured energy distribution of the electron beam at the extraction voltages (V_a-V_c) of 6.6 V, (a) V_c - I_{target} relation the different sample bias voltage V_{bias} and (b) the first derivative of I_{target}. From the observed data, we evaluated (c) maximum I_{target}, (d) FWHM of the energy spread ΔE_k and (e) the peak energy of the first derivative of I_{target}. The extraction voltages (V_a-V_c) were 4.8, 6.6 and 9.5 V.

4. Performance of AR-LEIPS apparatus

We tested the performance of the AR-LEIPS apparatus equipped with the electron gun described above. For this purpose, we measured the image potential state of the HOPG surface. This state gives a narrow peak approximately 1 eV below the vacuum level and has a free-electron-like nature along the surface, which means that the E-$k_{//}$ dispersion relation is expressed as,

$$E_b = \frac{\hbar^2 k_{||}^2}{2m^*} + (\text{constant}) \quad (3)$$

where m^* is the effective mass of the electron. We systematically investigated the E-$k_{//}$ dispersion at different photon energies $h\nu$ with a focus on the evaluation of the lowest limit of E_k in the AR-LEIPS measurement.

Figure 5a shows the AR-LEIPS spectra measured at $h\nu$ of 2.86 eV and 4.83 eV. We were particularly concerned about the electron behavior at the lowest electron energy E_k of around 2 eV. In LEIPS (and also AR-LEIPS), E_k for the image potential state can be varied by changing the bandpass filter, i.e., the photon energy $h\nu$. Good agreement between the two series of AR-LEIPS spectra confirms that the AR-LEIPS spectra can be measured even at the electron energy E_k of 2 eV. Note that the peak widths are broader in the spectra measured at 4.83 eV because the energy width of the 4.83 eV bandpass filter is larger (see ΔE_{ph} in Table 1).

In Figure 5b, the peak energies of the spectra measured at $h\nu$ of 4.83, 3.71, and 2.86 eV are plotted against $k_{//}$, which is converted according to Equation 2. The E-$k_{//}$ dispersion is well described by a quadratic relation with m^* of $1.2m_0$. This value is consistent with the reported ones of $1.2m_0$ to $1.3m_0$ by AR-IPES,[53–55] and $0.99 \pm 0.01m_0$ by two-photon photoelectron spectroscopy.[56] The E-$k_{//}$ relation is not dependent on $h\nu$. We conclude that AR-LEIPS can be measured with E_k as low as 2.0 eV and $k_{//}$ in the range of -3 to 5 nm^{-1}.

As we were able to confirm that we could quantitatively measure the energy and the wavelength, we evaluated the overall energy resolution ΔE_{total}, the energy spread of electron ΔE_k, and the angular spread of electron $\Delta\theta$. The overall energy resolution ΔE_{total} is the convolution of the resolution of the photon detector ΔE_{ph} and the energy spread of electron ΔE_k. ΔE_k is mainly determined by the thermal spread of electron $2k_BT$, where k_B and T are the Boltzmann constant and the absolute temperature of the cathode, respectively. T is typically 1150 K for the BaO cathode, giving the thermal energy spread of electrons of 0.2 eV. Provided that the observed peak width is sufficiently larger than the intrinsic width of the image potential state, we can assume that the peak width of the image potential state at $k_{//} = 0$ is determined by ΔE_k and ΔE_{ph}, i.e., expressed by $(\Delta E_k^2+\Delta E_{ph}^2)^{1/2}$. Specifically in the image potential state of HOPG, the peak width is further broadened by $\Delta k_{//}$ at a higher $k_{//}$ through the error propagation in Equation 3,

$$\Delta E(\text{owing to } \Delta k_{||}) \approx \frac{\partial E}{\partial k}\Delta k_{||} = \frac{\hbar^2 k_{||}}{m^*}\Delta k_{||}\,. \tag{4}$$

Therefore, ΔE_{total} is the convolution of the three contributions, ΔE_{k}, ΔE_{ph}, and $\Delta k_{//}$,

$$\Delta E_{\text{total}}^2 = \Delta E_{\text{k}}^2 + \Delta E_{\text{ph}}^2 + \left(\frac{\hbar^2 \Delta k_{||}}{m^*} k_{||}\right)^2 \tag{5}$$

In Figure 5c, $\Delta E_{\text{total}}^2$ is plotted against $k_{//}^2$. From the slope and the intercept, $\Delta k_{//}$ and $\Delta E_{\text{k}}^2+\Delta E_{\text{ph}}^2$ are obtained, respectively. As $k_{//}$ and θ are related by Equation 2, the angular spread of electron $\Delta\theta$ can be calculated from $\Delta k_{//}$. We use the value at $\theta = 0$ and estimate $\Delta\theta$ from the following relation derived from Equation 2,

$$\Delta\theta \approx \frac{\hbar}{\sqrt{2m_0 E_k}}\Delta k_{||} \tag{6}$$

As we separately determined ΔE_{ph} from the UV-vis measurements of the individual bandpass filters, ΔE_{k} can be evaluated. The obtained energy, angular resolutions and sample current are summarized in Table 1. The overall energy resolution ΔE_{total} is in the range between 0.2 and 0.3 eV depending on the ΔE_{ph} of the bandpass filter, and is similar to our previous report.[41] The angular spread of electron $\Delta\theta$ is dependent on E_{k} and is approximately 7° at E_{k} = 2–3 eV and improved to 5° at 4 eV. Donath and coworkers examined the angular spread of the electron gun by analyzing the Shockley surface state of Cu(111) and reported $\Delta\theta$ to be 3.9 ± 0.5° at E_{k} around 5 eV.[57] Considering that the electron beam is broadened at lower E_{k}, the performance of our electron gun is reasonable. Despite the slightly lower angular resolution $\Delta\theta$, the *k*-resolution is acceptable because of the low E_{k} ranging between 2 and 5 eV.

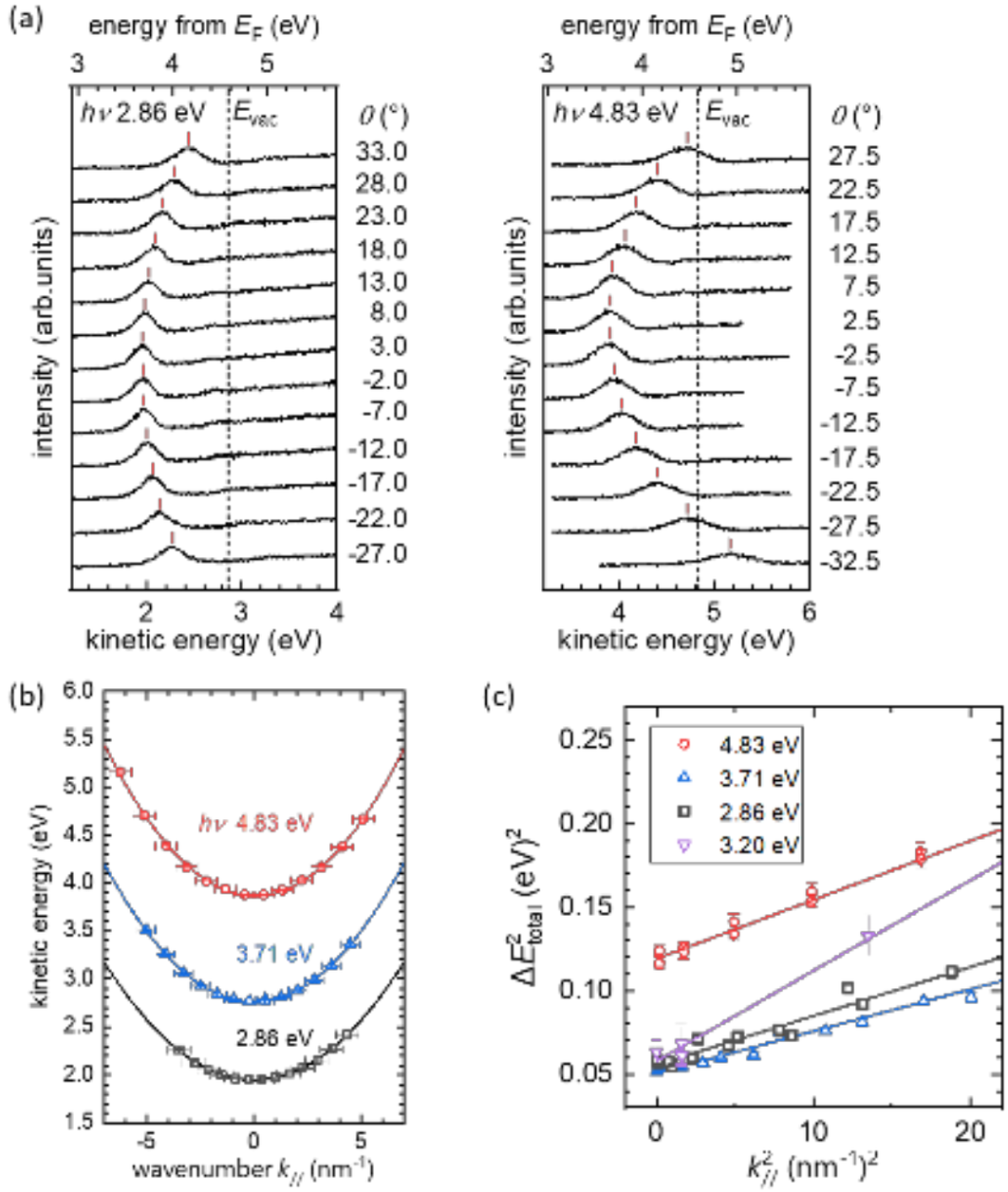

Figure 5. AR-LEIPS results of HOPG. (a) AR-LEIPS spectra measured at the photon energies $h\nu$ = 2.86 eV and 4.83 eV. Bars show the peak positions, and the vertical dashed lines indicate the vacuum level, E_{vac}. (b) E-$k_{//}$ dispersion relation measured at different photon energies. (c) The relationship between the peak widths and wavenumber is used to evaluate the energy and angular spreads from Equation 5 (see text).

Table 1. Energy resolution parameters obtained by analyzing the peak width of the image potential state of HOPG measured at different photon energies $h\nu$. The electron kinetic energy E_k is related to $h\nu$ by the relation $E_k = h\nu - 0.9$ eV.

photon detection (eV)		energy resolution at $\theta = 0^o$ (eV)		angular spread of electron		Sample current
energy $h\nu$	bandwidth ΔE_{ph}	total resolution ($(\Delta E_k^2 + \Delta E_{ph}^2)^{1/2}$)	energy spread of electron ΔE_k	Δk (nm^{-1})	$\Delta\theta$ (deg)	I_s (μA)
2.86	0.104	0.236 ± 0.003	0.212 ± 0.003	1.07 ± 0.05	8.6 ± 0.4	0.36
2.86	0.104	0.256 ± 0.039	0.215 ± 0.050	0.82 ± 0.08	6.5 ±0.6	0.19
3.20	0.117	0.241 ± 0.028	0.212 ± 0.030	0.95 ± 0.02	7.0 ±0.2	0.17
3.71	0.087	0.225 ± 0.002	0.207 ± 0.002	0.85 ± 0.02	5.7 ± 0.1	0.36
4.13	0.137	0.199 ± 0.063	0.145 ± 0.080	1.01 ± 0.07	6.8 ±0.4	0.14
4.83	0.282	0.342 ± 0.003	0.193 ± 0.005	1.02 ± 0.02	5.8 ± 0.1	0.24
4.83	0.282	0.341 ± 0.016	0.184 ± 0.03	0.92 ± 0.06	5.0 ± 0.3	0.20
average		0.23[a]	0.21	0.94 ± 0.02	5.9 ± 0.2	0.24

a) averaged value except for the data at the photon energy of 4.83 eV

5. Electron irradiation damage to organic samples

Finally, we discuss the irradiation damage to organic samples during the AR-LEIPS measurement. At first, we consider the minimum electron dose to obtain AR-LEIPS data of sufficient quality. The required quality of the data is dependent on the band structure

of the specific material. When the band consists of a single peak like the image potential state of HOPG (Figure 5a), the peak energy can be precisely determined even from a noisy spectrum. On the other hand, high-quality data are required when the peak consists of multiple components like the pentacene LUMO band (Figure 6a). For a stringent test, we chose a pentacene film on Cu(110) and examined the effect of electron irradiation.

Figure 6a shows the LEIPS spectra of pentacene as a function of electron dose. The negative second derivative of the spectrum shows a peak at 1.6 eV and a shoulder at 2.0 eV, as reported previously.[47] The position of the main peak can be readily determined from the spectrum of lowest quality at 0.8 mC. However, much higher quality data are required to resolve the two sub-bands contained in the LUMO-derived peak of pentacene. As shown in Figure 6b, we can clearly distinguish the two components above the electron dose of 3.0 mC.

Then, we examined the maximum-limiting dose for measuring LEIPS spectra without being affected by the electron irradiation. Figure 7(a) shows the LEIPS spectra at the Γ-point at higher electron doses than those shown in Figure 6. The electron current I_{target} was approximately 0.2 μA. The spectra showed no discernible changes up to the electron dose of 43.3 mC. The negative second-derivative spectra (Figure 7b) show the two components. Although the peak position slightly varied owing to the low signal-to-noise ratio, the energies of both features were maintained until the electron irradiation of 43.3 mC. The results demonstrate that we can safely determine the energies of the two peaks up to ca. 40 mC for pentacene.

By combining the above two findings, we can estimate the number of spectra without the effect of damage brought about by the electron irradiation. When we merely need to determine a single peak position, we can observe more than 50 spectra. When a more precise analysis is required to resolve multiple features, we can acquire at least 13 spectra. Among known organic materials, pentacene shows moderate durability against electron irradiation.[58] From the perspective of irradiation damage, the present LEIPS apparatus can examine the conduction band structures of most organic materials.

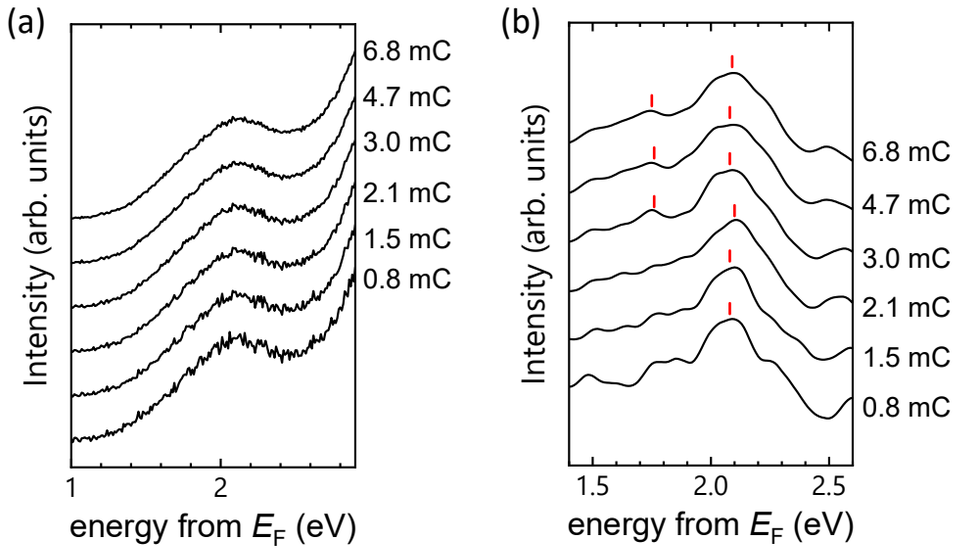

Figure 6. LEIPS spectra of a pentacene film with increasing electron dose to show the quality of the data (e.g., signal-to-noise ratio and appearance of the shoulder at 1.7 eV). The LEIPS spectra were measured at the electron incident angle θ of -10 deg. (a) Raw LEIPS spectra and (b) negative second-derivative spectra.

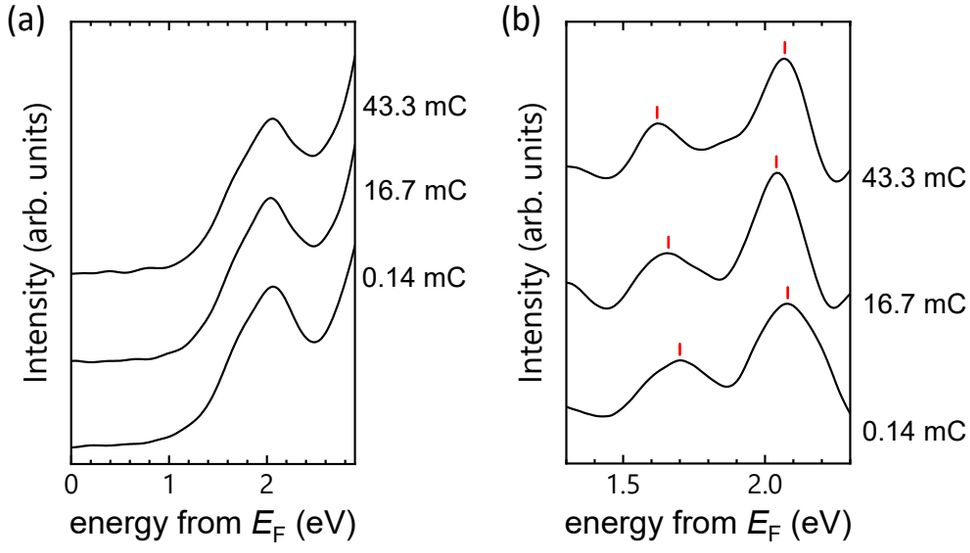

Figure 7. Effect of total amount of electron dose on (a) raw LEIPS spectra and (b) negative second-derivative spectra. The LEIPS spectra were measured at the electron incident angle θ of 0 deg (Γ-point).

6. Conclusion

We have developed an angle-resolved low-energy inverse photoelectron spectroscopy apparatus. The key challenge was to generate a low-energy electron beam with as low as E_k = 2 eV while maintaining the electron current at 0.2 μA or higher and the small energy and angular spread. For this purpose, we developed an electron gun with a four-element deceleration lens. In addition, the electrostatic and magnetic fields were carefully shielded. The performance was evaluated from the measurements of the image potential state of HOPG. By changing the photon energy, we confirmed that the AR-LEIPS measurements are possible at least from E_k of 2 eV to 5 eV with θ up to 32.5° (corresponding to $k_{//}$ up to 6.25 nm^{-1}). Because of the low E_k, the range of $k_{//}$ is limited but sufficiently large to cover the first Brillouin zone of most organic semiconductors. The overall energy resolution is 0.23 eV, and the angular spread of electron (full width) is 6°, which corresponds to $\Delta k_{//}$= 0.94 nm^{-1}. We compared the effect of irradiation damage and the quality of the spectral line shapes as a function of electron dose. The results confirmed that the present AR-LEIPS apparatus shows satisfactory performance with regard to observing conduction bands of functional materials without damaging the materials. This apparatus is particularly suitable for examining the conduction band structures of functional materials such as organic semiconductors[47] and organic-inorganic hybrid perovskites.[46]

Acknowledgments

This research was supported by JSPS KAKENHI (Grant Numbers 26288007 and 21H01902). H.S. thanks the JST SPRING grant (JPMJSP2109) for financial support.

Author Declarations

The authors have no conflicts of interest to disclose.

Author Contributions

HY conceptualized this work and designed most components of the apparatus including the electron gun and the optical system. YK, SI, and HS constructed most of the apparatus. YK and SI performed the electron ray-tracing. YK developed the electronics and the software. SI designed the manipulator and the sample holders. KK designed the Cu shielding cell. YK, SI, HS, HO, and KK performed the measurements. YK, HS, and HY analyzed the data. YK, HS, and HY wrote the manuscript. YK, SI, and HS contributed equally to this work.

Data Availability

The data that support the findings of this study are available from the corresponding author upon reasonable request.

References

1 S. Hüfner, *Photoelectron Spectroscopy: Principles and Applications* (Springer, Berlin, 2013).

2 V. Dose, "*Momentum-resolved inverse photoemission*", Surf. Sci. Rep. **5**, 337 (1985).

3 N. V. Smith, "*Inverse photoemission*", Rep. Prog. Phys. **51**, 1227 (1988).

4 P. D. Johnson and S. L. Hulbert, "*Inverse photoemission*", Rev. Sci. Instrum. **61**, 2277 (1990).

5 J. Rogozik, J. Küppers, and V. Dose, "*2π levels of CO and NO adsorbed at Pd(100) surfaces*", Surf. Sci. **148**, L653 (1984).

6 W. Reimer, T. Fink, and J. Küppers, "*Inverse photoemission spectroscopy of H, CO and NO adsorbed at Ni(100) and Ni(111) surfaces*", Surf. Sci. **193**, 259 (1988).

7 G. Rangelov, N. Memmel, E. Bertel, and V. Dose, "*Inverse photoemission study of carbon monoxide bonding to transition metals*", Surf. Sci. **251**–**252**, 965 (1991).

8 J. B. Pendry, "*New probe for unoccupied bands at surfaces*", Phys. Rev. Lett. **45**, 1356 (1980).

9 K. Tsutsumi, H. Yoshida, and N. Sato, "*Unocupied electronic states in a hexatriacontane thin film studied by inverse photoemission spectroscopy*", Chem. Phys. Lett. **361**, 367 (2002).

10 Z. Li, S. Sun, X. Li, and R. Schlaf, "*The impact of inverse photoemission spectroscopy measurements on regioregular poly(3-hexylthiophene) films*", Appl. Phys. Lett. **104**, 021606 (2014).

11 V. Dose, "*VUV isochromat spectroscopy*", Appl. Phys. **14**, 117 (1977).

12 G. Denninger, V. Dose, and H. Scheidt, "*A VUV isochromat spectrometer for surface analysis*", Appl. Phys. **18**, 375 (1979).

13 V. Dose, "*Ultraviolet Bremsstrahlung spectroscopy*", Prog. Surf. Sci. **13**, 225 (1983).

14 D. Funnemann and H. Merz, "*10 eV photon detector for inverse photoemission*", J. Phys. E. **19**, 554 (1986).

15 J. A. Lipton-Duffin, A. G. Mark, and A. B. McLean, "*Photon detection with n-propanol and C2H6O isomers*", Rev. Sci. Instrum. **73**, 3149 (2002).

16 J. A. Lipton-Duffin, A. G. Mark, G. K. Mullins, G. E. Contant, and A. B. McLean, "*An inverse photoemission system with large solid angle of detection and adjustable optical bandpass*", Rev. Sci. Instrum. **75**, 445 (2004).

[17] S. Banik, A. K. Shukla, and S. R. Barman, "*Optimal operating conditions and characteristics of acetone/CaF 2 detector for inverse photoemission spectroscopy*", Rev. Sci. Instrum. **76**, 066102 (2005).

[18] R. Stiepel, R. Ostendorf, C. Benesch, and H. Zacharias, "*Vacuum ultraviolet photon detector with improved resolution for inverse photoemission spectroscopy*", Rev. Sci. Instrum. **76**, 063109 (2005).

[19] M. Budke, V. Renken, H. Liebl, G. Rangelov, and M. Donath, "*Inverse photoemission with energy resolution better than 200 meV*", Rev. Sci. Instrum. **78**, 83903 (2007).

[20] M. Maniraj, S. W. D'Souza, J. Nayak, A. Rai, S. Singh, B. N. R. Sekhar, and S. R. Barman, "*High energy resolution bandpass photon detector for inverse photoemission spectroscopy*", Rev. Sci. Instrum. **82**, 93901 (2011).

[21] M. Maniraj, B. N. R. Sekhar, and S. R. Barman, "*Note: Characterization of CaF 2/acetone bandpass photon detector with Kr filter gas*", Rev. Sci. Instrum. **83**, 046107 (2012).

[22] N. Babbe, W. Drube, I. Schafer, and M. Skibowski, "*A simple and compact system for combined angular resolved inverse photoemission and photoemission in the vacuum ultraviolet*", J. Phys. E. **18**, 158 (1985).

[23] W. Sheils, R. C. G. Leckey, and J. D. Riley, "*Solid-state bandpass detector for inverse photoemission spectroscopy*", Rev. Sci. Instrum. **64**, 1194 (1993).

[24] K. Yokoyama, K. Nishihara, K. Mimura, Y. Hari, M. Taniguchi, Y. Ueda, and M. Fujisawa, "*Bandpass photon detector for inverse photoemission spectroscopy*", Rev. Sci. Instrum. **64**, 87 (1993).

[25] H. Namatame, M. Tamura, M. Nakatake, H. Sato, Y. Ueda, M. Taniguchi, and M. Fujisawa, "*High-resolution band-pass photon detector for inverse-photoemission spectroscopy*", J. Electron Spectros. Relat. Phenom. **80**, 393 (1996).

[26] F. Schedin, G. Thornton, and R. I. G. Uhrberg, "*Windows and photocathodes for a high resolution solid state bandpass ultraviolet photon detector for inverse photoemission*", Rev. Sci. Instrum. **68**, 41 (1997).

[27] G. Chauvet and R. Baptist, "*Inverse photoemission spectrometer in the range 20-100 eV*", J. Electron Spectros. Relat. Phenom. **24**, 255 (1981).

[28] T. Fauster, F. J. Himpsel, J. J. Donelon, and A. Marx, "*Spectrometer for momentum-resolved bremsstrahlung spectroscopy*", Rev. Sci. Instrum. **54**, 68 (1983).

[29] T. Fauster, D. Straub, J. J. Donelon, D. Grimm, A. Marx, and F. J. Himpsel, "*Normal-incidence grating spectrograph with large acceptance for inverse*

photoemission", Rev. Sci. Instrum. **56**, 1212 (1985).

30 P. T. Andrews, "*Inverse photoemission*", Vacuum **38**, 257 (1988).

31 M. Sancrotti, L. Braicovich, C. Chemelli, F. Ciccacci, E. Puppin, G. Trezzi, and E. Vescovo, "*Ultraviolet inverse photoemission spectrograph with parallel multichannel isochromat acquisition*", Rev. Sci. Instrum. **62**, 639 (1991).

32 P. D. Johnson, S. L. Hulbert, R. F. Garrett, and M. R. Howells, "*Normal incidence grating spectrometer designed for inverse photoemission studies in the range 10-30 eV*", Rev. Sci. Instrum. **57**, 1324 (1986).

33 Y. Gao, M. Grioni, B. Smandek, and J. H. Weaver, "*Inverse photoemission spectrometer for interface studies*", J. Phys. E. **21**, 489 (1988).

34 T. E. Ollonqvist and I. J. Väyrynen, "*Normal incidence grating spectrometer for inverse photoemission*", Vacuum **46**, 1177 (1995).

35 L. Kipp, M. Boehme, H. Carstensen, R. Claessen, and M. Skibowski, "*Compact grating spectrometer for inverse photoemission spectroscopy*", Rev. Sci. Instrum. **68**, 2144 (1997).

36 W. A. Royer and N. V. Smith, "*Refracting instrument for ultraviolet inverse photoemission spectroscopy*", Rev. Sci. Instrum. **59**, 737 (1988).

37 M. Nakatake, Y. Okamura, S. Akiyama, H. Namatame, and M. Taniguchi, "*High-resolution photon detection system for inverse-photoemission spectroscopy*", J. Electron Spectros. Relat. Phenom. **88**–**91**, 1027 (1998).

38 N. Ueno and S. Kera, "*Electron spectroscopy of functional organic thin films: Deep insights into valence electronic structure in relation to charge transport property*", Prog. Surf. Sci. **83**, 490 (2008).

39 H. Yoshida, "*Near-ultraviolet inverse photoemission spectroscopy using ultra-low energy electrons*", Chem. Phys. Lett. **539**–**540**, 180 (2012).

40 H. Yoshida, "*Measuring the electron affinity of organic solids: An indispensable new tool for organic electronics*", Anal. Bioanal. Chem. **406**, 2231 (2014).

41 H. Yoshida, "*Principle and application of low energy inverse photoemission spectroscopy: A new method for measuring unoccupied states of organic semiconductors*", J. Electron Spectros. Relat. Phenom. **204**, 116 (2015).

42 B. Boudaïffa, P. Cloutier, D. Hunting, M. A. Huels, and L. Sanche, "*Resonant formation of DNA strand breaks by low-energy (3 to 20 eV) electrons*", Science **287**, 1658 (2000).

43 M. V. Muftakhov, R. V. Khatymov, and R. F. Tuktarov, "*Decomposition of Aromatic Compounds Relevant to Organic Electronics under Exposure to Low-Energy Electrons*", Tech. Phys. **63**, 1854 (2018).

[44] A. Kahn, N. Koch, and W. Gao, "*Electronic structure and electrical properties of interfaces between metals and π-conjugated molecular films*", J. Polym. Sci., B Polym. Phys. **41**, 2529 (2003).

[45] H. Yoshida, "*Low-energy inverse photoemission spectroscopy using a high-resolution grating spectrometer in the near ultraviolet range*", Rev. Sci. Instrum. **84**, 103901 (2013).

[46] J. Yang, H. Sato, H. Orio, X. Liu, M. Fahlman, N. Ueno, H. Yoshida, T. Yamada, and S. Kera, "*Accessing the Conduction Band Dispersion in $CH_3NH_3PbI_3$ Single Crystals*", J. Phys. Chem. Lett. **12**, 3773 (2021).

[47] H. Sato, S. A. Syed, Y. Yamada, H. Ishii, and H. Yoshida, "*Conduction band structure of high-mobility organic semiconductors and partially dressed polaron formation*", Nat. Mater. **21**, 910 (2022).

[48] K. Desinger, V. Dose, M. Göbl, and H. Scheidt, "*Momentum resolved bremsstrahlung isochromat spectra from Ni(0 0 1)*", Solid State Commun. **49**, 479 (1984).

[49] H. Yoshida, "*Note: Low energy inverse photoemission spectroscopy apparatus*", Rev. Sci. Instrum. **85**, 016101 (2014).

[50] P. W. Erdman and E. C. Zipf, "*Low-voltage, high-current electron gun*", Rev. Sci. Instrum. **53**, 225 (1982).

[51] N. G. Stoffel and P. D. Johnson, "*A low-energy high-brightness electron gun for inverse photoemission*", Nucl. Instrum. Methods A **234**, 230 (1985).

[52] C. D. Child, "*Discharge from hot cao*", Phys. Rev. (Series I) **32**, 492 (1911).

[53] I. Schäfer, M. SchİIter, and M. Skibowski, "*Conduction-band structure of graphite studied by combined angle-resolved inverse photoemission and target current spectroscopy*", Phys. Rev. B **35**, 7663 (1987).

[54] R. Claessen, H. Carstensen, and M. Skibowski, "*Conduction-band structure of graphite single crystals studied by angle-resolved inverse photoemission and target-current spectroscopy*", Phys. Rev. B **38**, 12582 (1988).

[55] F. Maeda, T. Takahashi, H. Ohsawa, S. Suzuki, and H. Suematsu, "*Unoccupied-electronic-band structure of graphite studied by angle-resolved secondary-electron emission and inverse photoemission*", Phys. Rev. B **37**, 4482 (1988).

[56] K. Takahashi, J. Azuma, and M. Kamada, "*Two-dimensional band dispersion and momentum-resolved lifetime of the image-potential state on graphite studied by angle-resolved multiphoton photoemission spectroscopy*", Phys. Rev. B **85**, 075325 (2012).

[57] A. Zumbülte, A. B. Schmidt, and M. Donath, "*Momentum resolution in inverse photoemission*", Rev. Sci. Instrum. **86**, 013908 (2015).

[58] L. Reimer, Chapter 10 in *Transmission Electron Microscopy: Physics of Image Formation and Microanalysis* (Springer, New York, 1997).

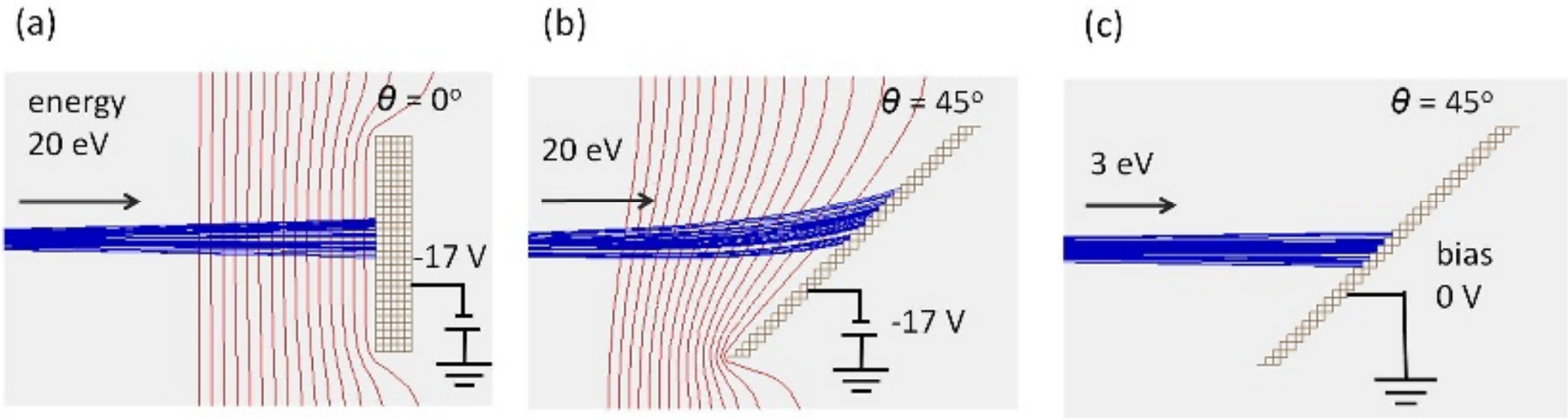
(a)
energy
20 eV
θ = 0°
-17 V
(b)
20 eV
θ = 45°
-17 V
(c)
θ = 45°
3 eV
bias
0 V

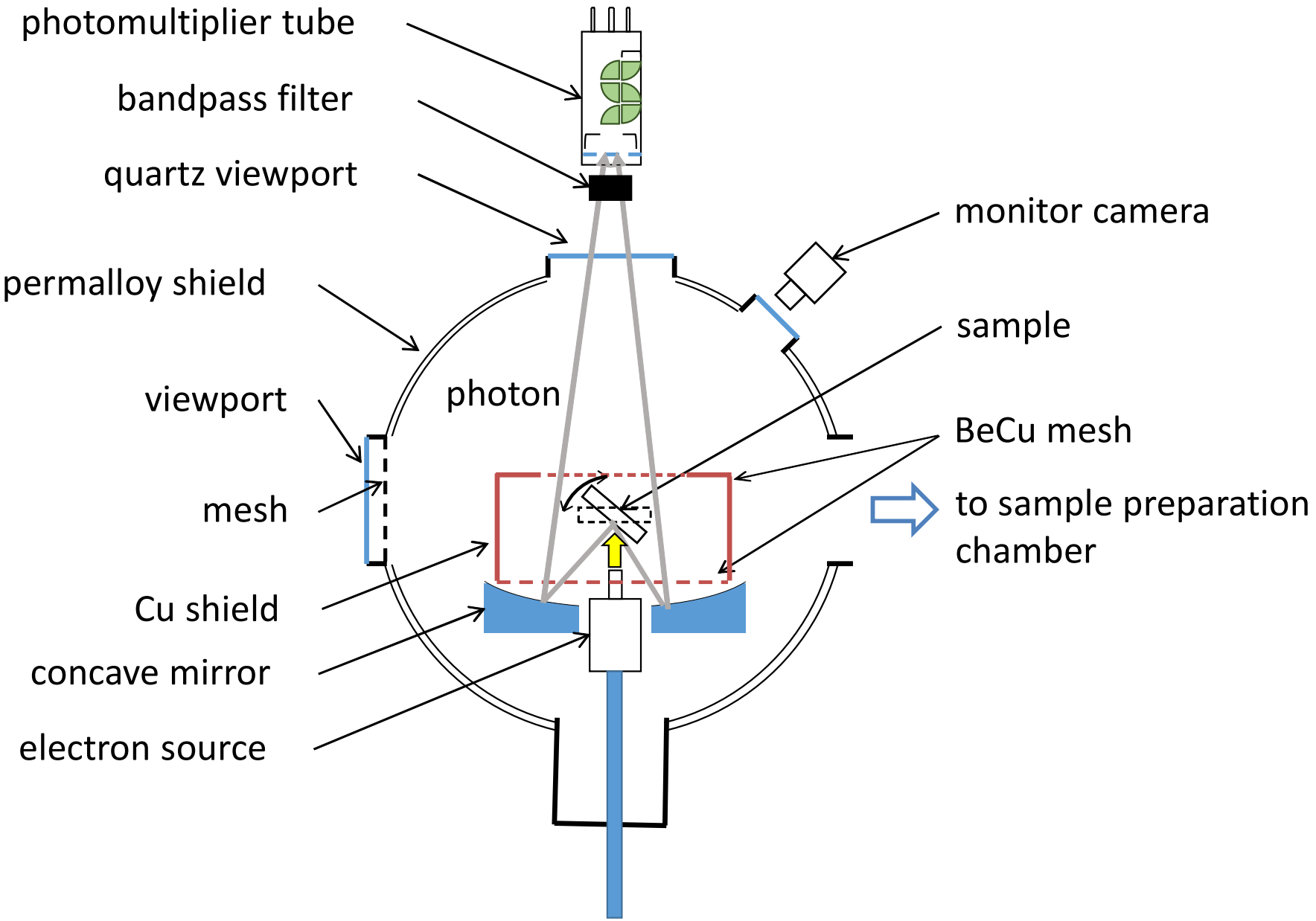
photomultiplier tube
bandpass filter
quartz viewport
permalloy shield
viewport
mesh
Cu shield
concave mirror
electron source
photon
monitor camera
sample
BeCu mesh
to sample preparation chamber

(a)

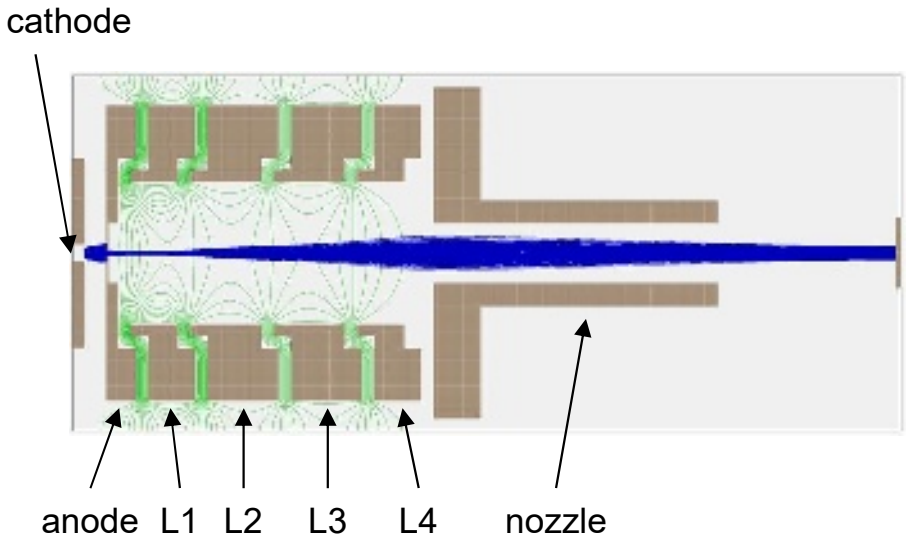
cathode
anode
L1
L2
L3
L4
nozzle

(b)

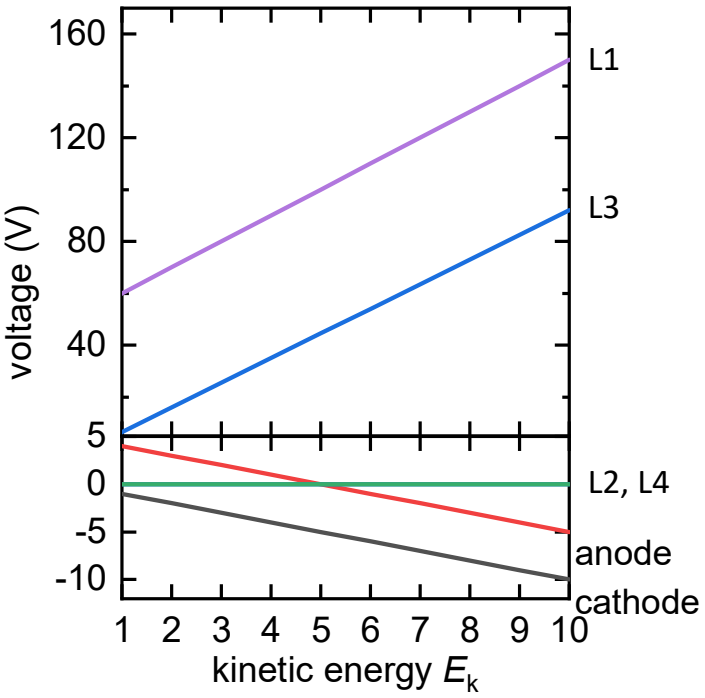
160
120
80
40
5
0
-5
-10
voltage (V)
L1
L3
L2, L4
anode
cathode
1 2 3 4 5 6 7 8 9 10
kinetic energy E_k

(c)

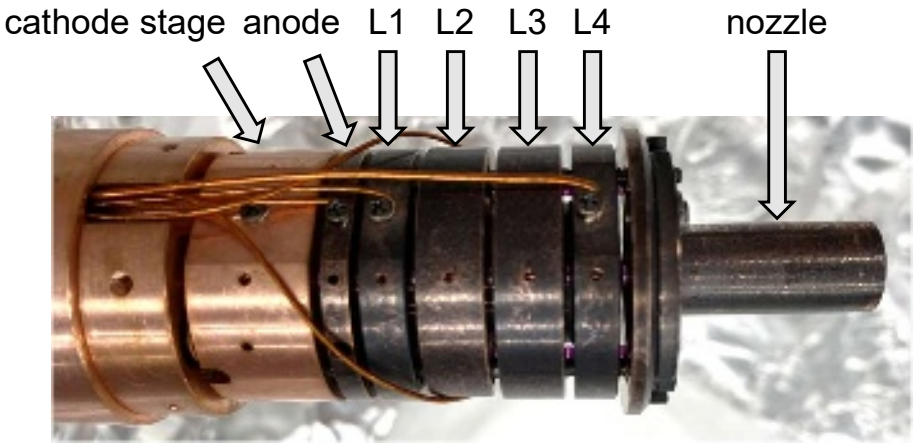
cathode stage
anode
L1
L2
L3
L4
nozzle

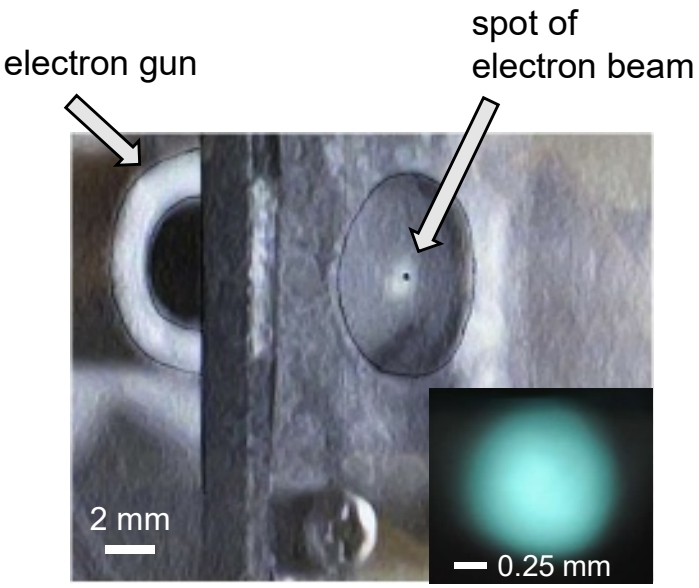
electron gun
spot of
electron beam
2 mm
0.25 mm

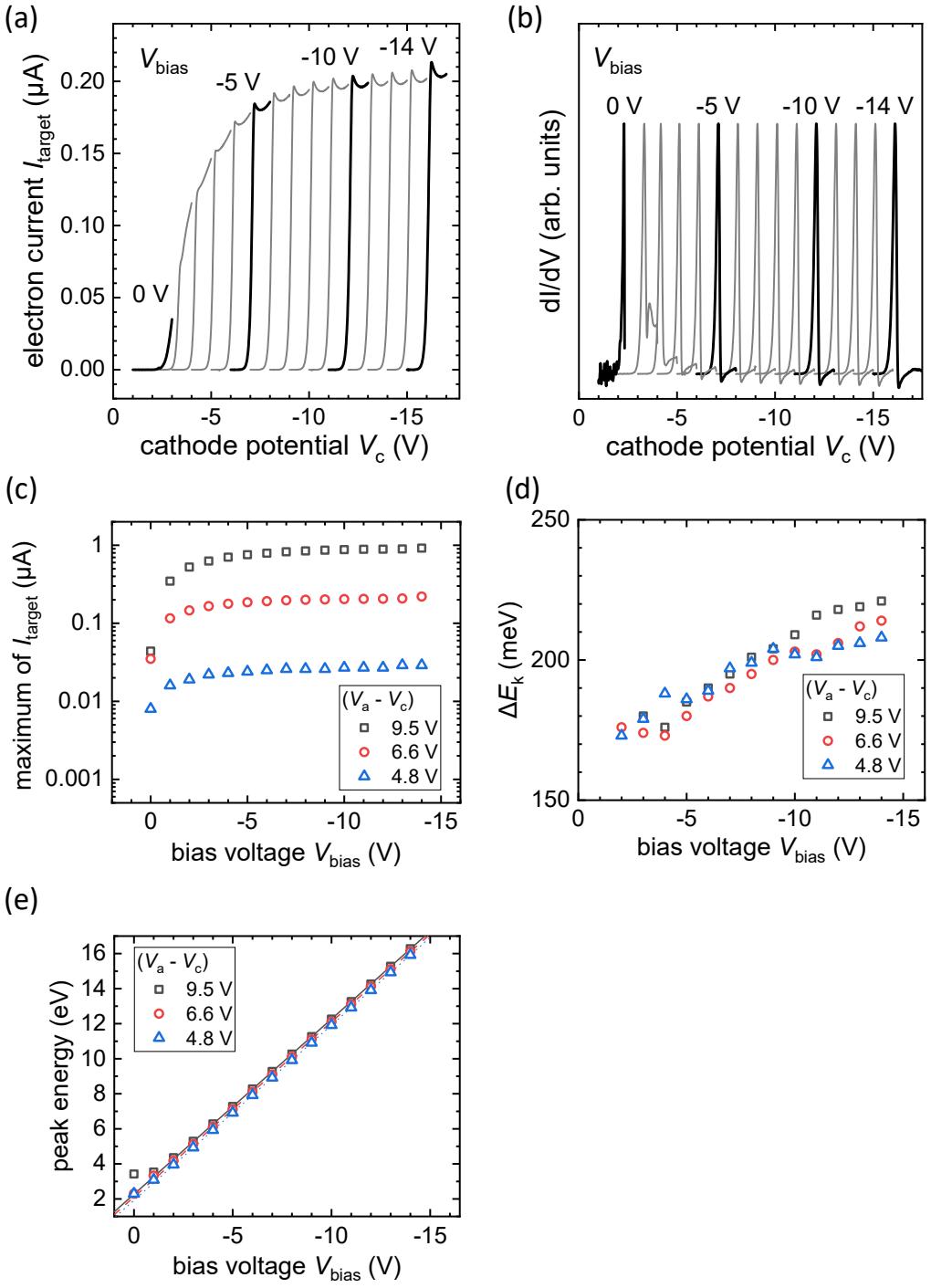
(a)
V_{bias}
0 V
-5 V
-10 V
-14 V
electron current I_{target} (μA)
0.20
0.15
0.10
0.05
0.00
0
-5
-10
-15
cathode potential V_c (V)
(b)
V_{bias}
0 V
-5 V
-10 V
-14 V
dI/dV (arb. units)
0
-5
-10
-15
cathode potential V_c (V)
(c)
maximum of I_{target} (μA)
1
0.1
0.01
0.001
$(V_a - V_c)$
9.5 V
6.6 V
4.8 V
0
-5
-10
-15
bias voltage V_{bias} (V)
(d)
ΔE_k (meV)
250
200
150
$(V_a - V_c)$
9.5 V
6.6 V
4.8 V
0
-5
-10
-15
bias voltage V_{bias} (V)
(e)
peak energy (eV)
16
14
12
10
8
6
4
2
$(V_a - V_c)$
9.5 V
6.6 V
4.8 V
0
-5
-10
-15
bias voltage V_{bias} (V)

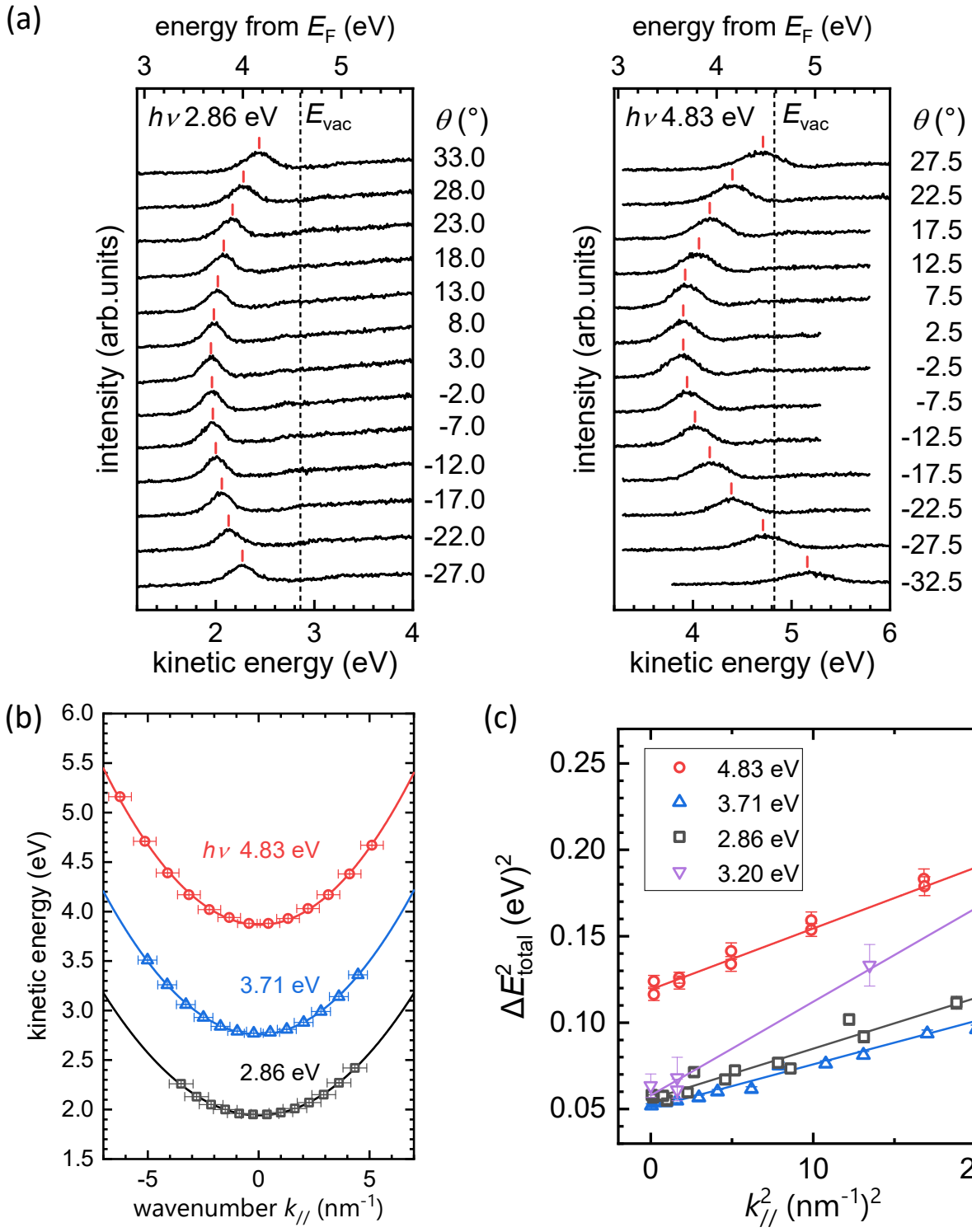
(a)
energy from E_F (eV)
3
4
5
$h\nu$ 2.86 eV
E_{vac}
θ (°)
33.0
28.0
23.0
18.0
13.0
8.0
3.0
-2.0
-7.0
-12.0
-17.0
-22.0
-27.0
intensity (arb.units)
2
3
4
kinetic energy (eV)
energy from E_F (eV)
3
4
5
$h\nu$ 4.83 eV
E_{vac}
θ (°)
27.5
22.5
17.5
12.5
7.5
2.5
-2.5
-7.5
-12.5
-17.5
-22.5
-27.5
-32.5
intensity (arb.units)
4
5
6
kinetic energy (eV)
(b)
6.0
5.5
5.0
4.5
4.0
3.5
3.0
2.5
2.0
1.5
kinetic energy (eV)
$h\nu$ 4.83 eV
3.71 eV
2.86 eV
-5
0
5
wavenumber $k_{//}$ (nm^{-1})
(c)
0.25
0.20
0.15
0.10
0.05
ΔE^2_{total} (eV)^2
4.83 eV
3.71 eV
2.86 eV
3.20 eV
0
10
20
$k^2_{//}$ (nm^{-1})^2

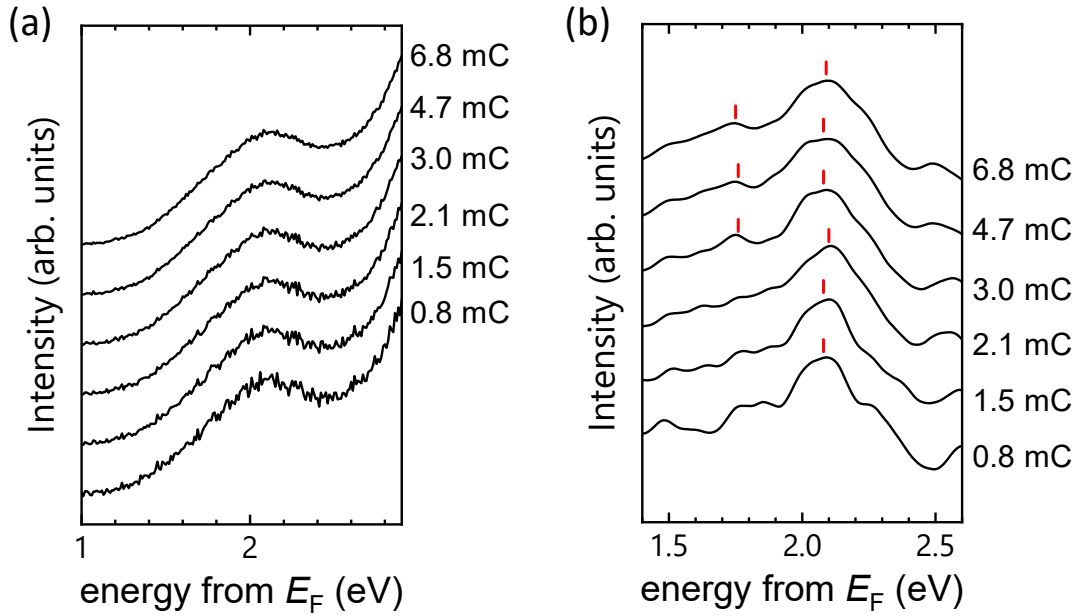
(a)
Intensity (arb. units)
6.8 mC
4.7 mC
3.0 mC
2.1 mC
1.5 mC
0.8 mC
1
2
energy from E_F (eV)
(b)
Intensity (arb. units)
6.8 mC
4.7 mC
3.0 mC
2.1 mC
1.5 mC
0.8 mC
1.5
2.0
2.5
energy from E_F (eV)

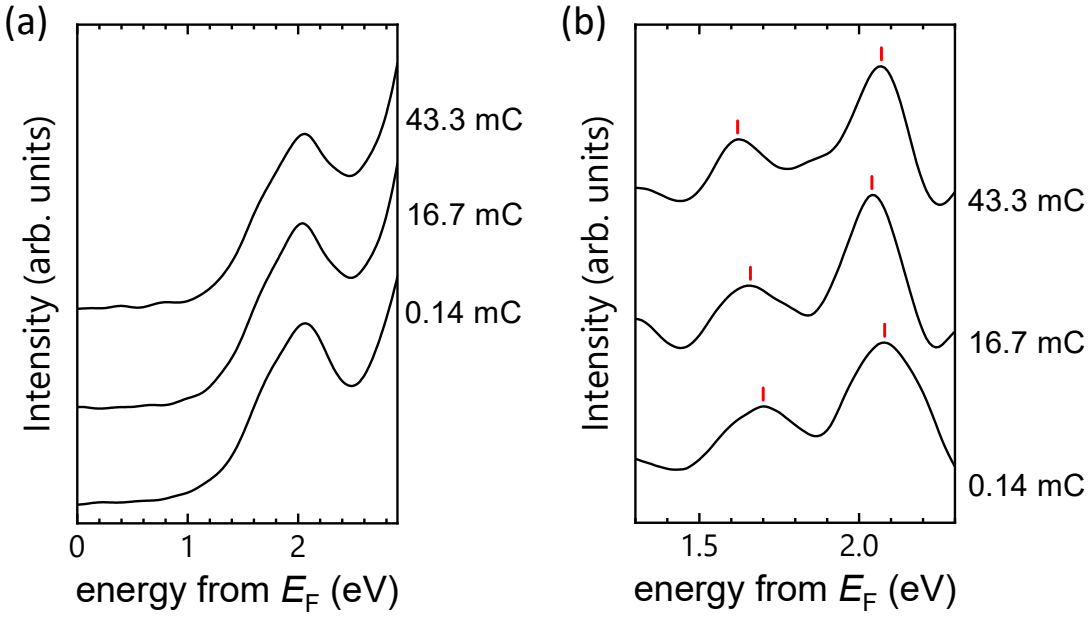
(a)
Intensity (arb. units)
43.3 mC
16.7 mC
0.14 mC
0
1
2
energy from E_F (eV)
(b)
Intensity (arb. units)
43.3 mC
16.7 mC
0.14 mC
1.5
2.0
energy from E_F (eV)